Coupled experimental and computational study of residual stresses of additively manufactured Ti-6Al-4V components

M. Strantza[1], R. K. Ganeriwala[2], B. Clausen[1], T. Q. Phan[3], L.E. Levine[3], D. Pagan[4], W. E. King[2], N. E. Hodge[2], D. W. Brown[1]

[1]Los Alamos National Laboratory
[2] Lawrence Livermore National Laboratory
[3] National Institute of Standards and Technologies
[4]Cornell High Energy Synchrotron Source

Abstract

The production of metallic parts via laser-powder bed fusion (L-PBF) additive manufacturing is rapidly growing. To use components produced via L-PBF in safety-critical applications, a high degree of quality confidence is required. This qualification can be supported by means of a validated thermomechanical model capable of predicting the final residual stress state and subsequent lifetime. In this work, we use high-energy X-ray diffraction to determine a three-dimensional residual strain and stress state of a Ti-6Al-4V L-PBF component. The experimental results are used to aid in validation of simulations. Strong agreement is observed between the experiments and the model predictions.

Additive manufacturing (AM), commonly called 3D printing, has been progressively gaining momentum during the past decade as an innovative fabrication technology [1]. As opposed to conventional subtractive manufacturing techniques, AM has the ability to create complex and lightweight geometrical structures with a high level of flexibility and minimal waste [2–4]. A wide range of different AM technologies exists. One of the main AM processes for the production of metal components is laser-powder bed fusion (L-PBF). This process uses a high power-density laser to selectively melt and fuse the metallic particles together layer-by-layer. However, the thermal history of L-PBF components results in the formation of unwanted and, frequently, detrimental residual stresses [5],[6]. For example, high tensile residual stresses at a surface can cause crack initiation and lead to an early failure of the structure. Furthermore, the developed residual stresses may cause localized distortion that can jeopardize the net shape of the component.

Certainly, safety critical industrial applications demand a high degree of confidence with respect to the structural integrity of L-PBF components. Currently, there is a limited understanding of the residual stresses in AM components. This limitation has a critical impact on the usage of the AM metallic components, while it restrains the unique ability of process models to predict the final behavior of the AM structures. Since experimental measurement during processing is often not feasible, having a validated model capable of reliably simulating these stresses is extremely valuable. In that aspect, Lawrence Livermore National Laboratory (LLNL) has developed Diablo [7], a multiphysics finite element code capable of predicting residual stresses in AM components. In an effort to provide valuable experimental validation data for Diablo, high-energy X-ray diffraction measurements were performed on a sample that was produced via the L-PBF process. X-ray diffraction was used to accurately measure the lattice parameters, and then determine the elastic strains present in the Ti-6Al-4V components while still attached to the base plate. In this work, the experimental results of the three-dimensional residual strain state of L-PBF component will be qualitatively and quantitatively compared to the simulation predictions of Diablo.

For this investigation, a bridge-shaped Ti-6Al-4V specimen was produced by means of the L-PBF AM process using a Concept Laser M2 machine.[1] A laser power of 100 W and scan speed of 600 $^{mm}/_{s}$ were used for the processing conditions along with a layer thickness of 30 µm and track width of 150 µm. The Ti-6Al-4V sample, shown schematically in Figure 1, was built on a small Ti-6Al-4V build plate of 55 mm × 55 mm × 8 mm with no support structures. The Ti-6Al-4V specimen was built via a continuous scanning strategy aligned at 45° to the x-axis. A 90° rotation in scan orientation was performed after each layer.

The high-energy X-ray diffraction experiments were conducted on the A2 beamline at the Cornell High Energy Synchrotron Source (CHESS). The A2 beamline takes a polychromatic X-ray beam with effective spectrum from 50 keV to 150 keV produced by electrons passing through a 1.5 m CHESS Compact Undulator [9]. The incident X-ray beam was masked to a 0.2 mm × 0.2 mm cross-section by a pair of lead incident beam slits. The incident beam penetrated the Ti-6Al-4V sample and diffracted through two sets of slits with a fixed 2θ angle of 8°. Diffracted intensity was measured on a germanium, single element Canberra GL-0055 detector. The incoming bias voltage signal was supplied by an XIA DXP Saturn USB2 digital X-ray processor and the photon energy discrimination was performed on an XIA Mercury-1 digital X-ray processor.

The multiple slit geometry results in a 'rhomboidal' shaped diffraction volume of 0.2 mm × 1.5 mm × 0.2 mm, where the long dimension is along the incident beam direction. Depending on the orientation of the sample with respect to the beam, the 1.5 mm dimension of the diffraction volume was altered between the x and y dimension of the sample, as defined in Figure 1. In the case of the measurement of the x and z strain components, the 1.5 mm dimension was oriented along the 5 mm dimension (through-thickness) of the specimen. For the case of the y strain component the 1.5 mm diagonal is oriented along the 21 mm dimension of the sample. For the x and z strain components, measurements were collected every 0.5 mm and every 1mm for the y component.

It is important to mention that the alignment of the sample and the measurement locations were confirmed by using the transmitted beam data of the detector. The transmitted data are referring to the output of the diode that is located behind the sample during the measurements. The sample was positioned in a four-circle goniometer with built-in translation stages that enabled the automated rotation of the sample to collect diffraction data for the three orthogonal strain components (x, y and z). Individual diffraction patterns were collected from the xz cross-section at the center thickness of the sample (see blue plane located at y = 2.5 mm in Figure 1).

[1] Certain commercial entities, equipment, or materials may be identified in this document to describe an experimental procedure or concept adequately. Such identification is not intended to imply recommendation or endorsement by the National Institute of Standards and Technology, Los Alamos National Laboratory, or Lawrence Livermore National Laboratory, nor is it intended to imply that the entities, materials, or equipment are necessarily the best available for the purpose.

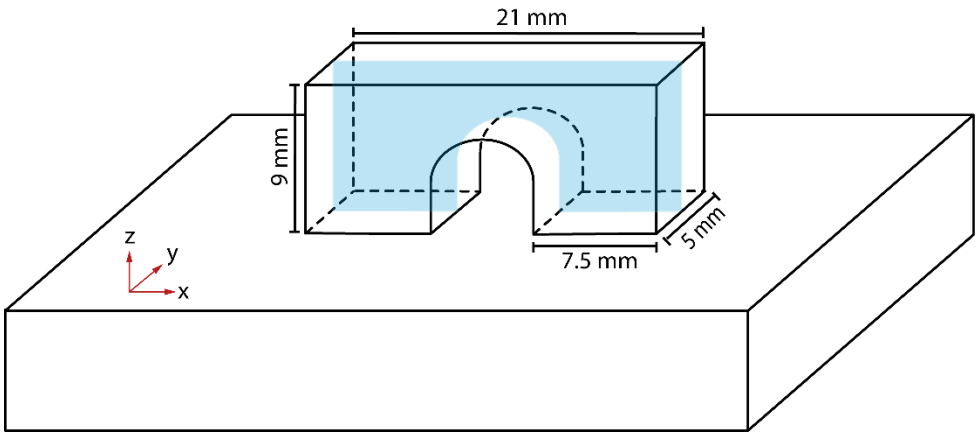

Figure 1: Schematic representation of the laser-powder bed fusion Ti-6Al-4V sample. The measurements were performed halfway through the thickness of the sample (the blue plane located at y = 2.5 mm)

A total of 2,000 1-D diffraction patterns collected on this sample were refined by using the automated SMARTSware [10] program to drive whole-pattern Rietveld analysis in the General Structural Analysis System (GSAS) software [11] developed at Los Alamos National Laboratory. A single phase hexagonal close packed crystal structure, assumed V supersaturated α′ [12], was used for the fit to determine the -a and -c lattice parameters at each measured position.

To determine the residual strain values, equation 1 is used

$$\varepsilon_a = \frac{a-a_0}{a_0}, \quad \varepsilon_c = \frac{c-c_0}{c_0}, \qquad \text{Eq. 1}$$

where a_0 and c_0 are the stress-free lattice parameter.

To this end, four reference samples were extracted along the height of an identical sample to take into account any possible microstructural variations through the part. Samples of 2 × 2 × 3 mm^3 were extracted via electric discharging machining (EDM) to eliminate the macroscopic residual stress field [3], allowing the stress free lattice parameters to be determined. The final strains are calculated using the averaged crystallographic strain given by $\bar{\varepsilon} = \frac{2\varepsilon_a+\varepsilon_c}{3}$ [13]. Note that in order to calculate the three main stress components, the strain measurements were interpolated in order to match the locations of the x, y and z strain components of Figure 2(a). Three orthogonal stress components can be calculated from the three orthogonal lattice strains in the x, y and z direction by using the general Hooke's law:

$$\sigma_i = \frac{E}{(1+\nu)(1-2\nu)}\Big((1-\nu)\varepsilon_i + \nu\big(\varepsilon_j + \varepsilon_k\big)\Big), \text{ where } i, j, k \in \text{x, y, z} \qquad \text{Eq. 2}$$

In Eq. 2, E represents Young's modulus and ν is Poisson's ratio. The Young's modulus and Poisson's ratio of similarly built Ti-6Al-4V are 115 GPa and 0.32, respectively [8]. However, it is important to note here that the assumption of isotropy when converting from strains to stress adds an additional degree of uncertainty, as it is commonly known that AM-built materials typically exhibit anisotropic material properties based upon the build direction. With respect to the modelling approach, due to the large range of time and length scales in the L-PBF process, simulating an entire build at the physical process scale is currently not computationally feasible. Thus, some type of strategy to speed up the computations was necessary. The authors built upon the approach of Hodge et al. [14,15] whereby multiple physical layers are lumped into one agglomerated computational layer and the beam spot size is similarly enlarged. In this work, 0.5 mm computational layers were used in conjunction with a 0.5 mm beam radius. Consequently,

the temperature history and spatial gradients are not fully captured. The fully coupled thermomechanical system was solved using the parallel, implicit Lagrangian finite element code Diablo.

An element activation technique is employed where a new layer of elements is activated at the beginning of each computational layer. These elements are initially assigned powder properties until they have been heated over the material's melting temperature, at which point they are given bulk material properties. The computational scan speed is held equal to the physical process value (600 $^{mm}/_{s}$), while the beam power is increased such that complete melting of the powder layer occurs. A constant temperature, Dirichlet boundary condition is applied to the bottom of the base plate. The heat source is modeled as a uniform volumetric heat input, applied to all integration points within the beam's radius on the layer actively being scanned. Although the physical process typically employs a Gaussian beam, the assumption of a uniform volumetric heat input is appropriate here since the true beam shape and exact heat profile gets lost as a result of the agglomeration methodology. The total amount of cooling time after each layer is scaled by the ratio of the computational powder layer depth to physical powder layer depth such that the total process time is kept constant.

Due to the significant dependence of the strength of Ti-6Al-4V on strain rate at elevated temperatures [16], a material model which best captures the behavior of the material during each of the relevant temperature regions was developed [17]. A rate independent plasticity model is used for $T < 0.5T_m$, a viscoplasticity model for $0.5T_m \leq T < 0.8T_m$, and a Maxwell-type viscoelasticity model (allowing for complete stress and plastic strain relaxation) when $T \geq 0.8T_m$. Here, T is the average temperature of an element and $T_m = 1923\ K$ is the melting temperature of Ti-6Al-4V. Finally, it is important to remark that surrounding powder was not included in the simulation to speed up computation time. Complete details regarding the implementation of this modeling approach, along with all temperature-dependent material properties and process parameters will be published in a follow up article.

Throughout this paper, the results will be presented by using a two-dimensional schematic representation of the xz plane of the sample. The experimental uncertainties, 100 με to 160 με in the x and z strains, and 120 με to 250 με in the y strain, are derived from the statistical estimated standard deviations of the Rietveld peak fitting. The increased uncertainty of the y strain component is associated with the longer sample path (≈ 21 mm) that the beam needs to traverse in order to collect the measurements. The associated stress uncertainties propagated from the statistical strain uncertainties are roughly ± 30 MPa. These uncertainties propagate into all three stress components. Therefore, to assess the comparison between experimental measurements and simulations, it is essential to use the individual resolution of the x, y and z strains.

Figure 2(a), shows contour plots of the observed x, y and z components of the residual strain. The plots show that for the z strain component, high tensile strains (up to 7,600 με) at the extreme sides (left and right) are balanced by compressive strains at the interior of the sample (to −5,300 με). The highest tensile strains are located at the left and right extreme sides of the sample. The x and y strain components are mainly under tensile strain for this cross-section. Based on the contour plot of the y strain component, the maximum strain (3,000 με to 3,700 με) is present along the perimeter of the arch and close to the top and the bottom of the sample. The x strain component indicates tensile strain values within the samples ranging between 70 με to 3,700 με. The maximum tensile values are found closer to the top and the bottom of the sample. At the areas close to the perimeter of the arch, the strains are mainly compressive (−2,500 με to −80 με) with some values that are close to zero. It is apparent from the plot that the x strain component also contains compressive residual strain at the extreme sides of the bridge (left and right side).

(a)

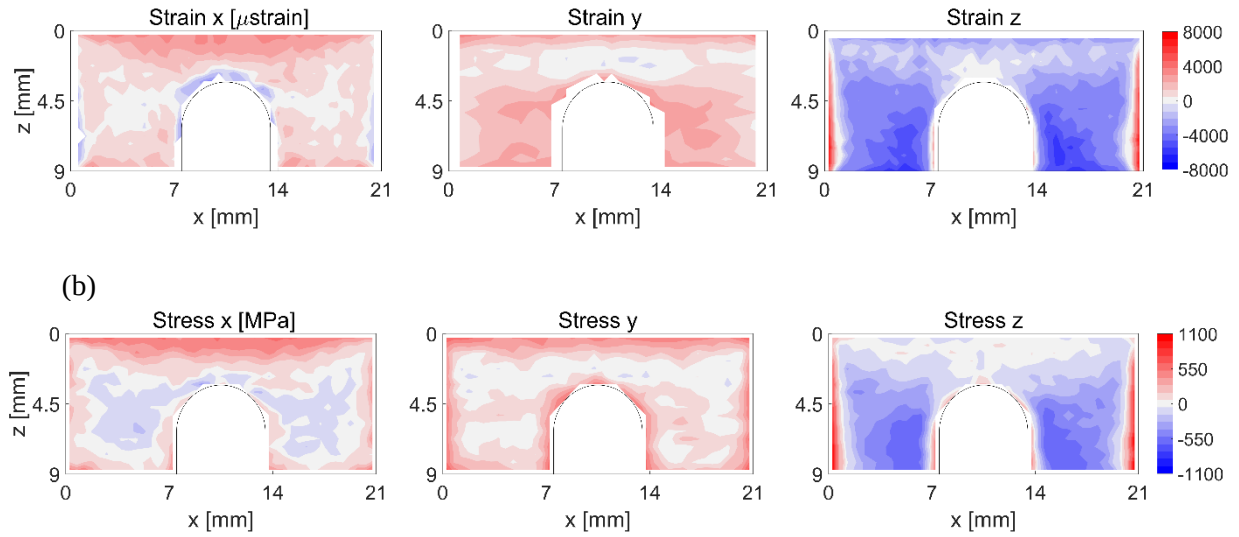

Figure 2: (a) Experimental residual strain maps over the investigated middle cross-section of the sample (y = 2.5 mm). Strains are shown in μstrain for the x, y and z strain components. (b) Experimental residual stress maps over the investigated middle cross-section of the sample. Stresses are shown in MPa.

The x, y and z components of the residual stress are shown in Figure 2(b). The residual stress distribution of the z orientation within the sample is generally compressive. The lowest compressive stress value of approximately −600 MPa is located within the legs of the bridge sample. At the top of the sample, the residual stresses are close to zero within the measurement uncertainty. There is an extended tensile region (1.25 mm away from the left and right side of the sample) that reaches a maximum value of 1,100 MPa (± 34 MPa); compared to the observed room temperature yield strength of AM Ti-6Al-4V (≈1,150 MPa) [8]. The stresses along the perimeter of the arch are also tensile with a maximum stress of 600 MPa (± 26 MPa). It is important to mention that the diffraction measurements are performed 0.25 mm away from the free surfaces, suggesting that the magnitude of the high tensile stresses could be even higher closer to the edges. Note that high tensile stresses at free surfaces are likely to contribute to crack initiation and eventually jeopardize the performance of an L-PBF component. In contrast, the x stress component contains tensile stresses along the perimeter of the sample with high residual stresses (630 MPa) being present at the regions close to the top of the sample. However, within the sample the stress is mainly compressive and close to zero. A similar trend is also present for the y stress component.

Clearly, the residual stress distribution of the x and y stress components is lower compared to the z component. It is apparent that in the case of the x stress, there is high tensile zone above the arch of the L-PBM sample. This tensile region (roughly about 550 MPa) indicates a high bending moment that could lead to the distortion of the sample when the sample is released from the substrate. The residual stress distribution of the y stress component is mainly tensile and does not exhibit a big variation, which is associated with the shorter side of the sample.

The experimental residual stress distribution that is presented in the current work is in line with results presented in the literature [18]. Generally, the residual stresses that are locked in a component must attain equilibrium between tension and compression. Consequently, the compressive residual stresses must be balanced by the tensile stresses over a given cross section. Moving from the bottom of the sample towards the top of the sample, it is apparent that the tensile region of the z stress component becomes thinner. Furthermore, the stresses closer to the substrate are larger compared to the stresses closer to the top of the sample, for example at z = 1.25 mm the z stress is ≈ 300 MPa while at z = 8.25 the stress is ≈ 1,047 MPa. At the locations close to the substrate, higher thermal gradients are present since the substrate acts as a heat sink resulting in higher residual stresses closer to the substrate. This suggests that the stresses are influenced by the height of the sample, or equivalently, by the number of the layers as shown in [19].

Figure 3(a) shows the residual strain predictions for the x, y and z strain components as revealed from the Diablo calculations. Note, that the predicted strains were extracted from the same measurement locations (see Figure 1) and were averaged over the same experimental diffraction volume. The highest tensile strain in the z component is present at the top of the part (≈ 3,700 με) and close to the baseplate (≈ 4,500 με) for the x component. High compressive regions are located at the edges of the sample (≈ −5,100 με) and on the area above and along the perimeter of the arch (≈ −1,300 με). The y strain component exhibits lower residual strains. At the top of the sample, y strains are close to zero (between 20 με and 250 με) with a compressive region (≈ −1,330 με) just above the arch of the bridge. The maximum tensile strain of ≈ 3,500 με is located at the regions close to the baseplate.

Figure 3(b) shows the residual stress predictions for the x, y and z stress components. The x stress component shows high tensile stresses (≈ 450 MPa) at the top of the sample and close to the base plate (≈ 750 MPa). The x stresses at the extreme sides of the sample are close to zero. Within the sample, the stresses are mainly compressive (≈ −250 MPa). For the y stress component, within the sample the stresses are mainly compressive and close to zero while tensile stresses can be found at the regions along the perimeter of the sample. Stresses along the build direction (z) indicate a similar distribution as in the cases of the z strain component.

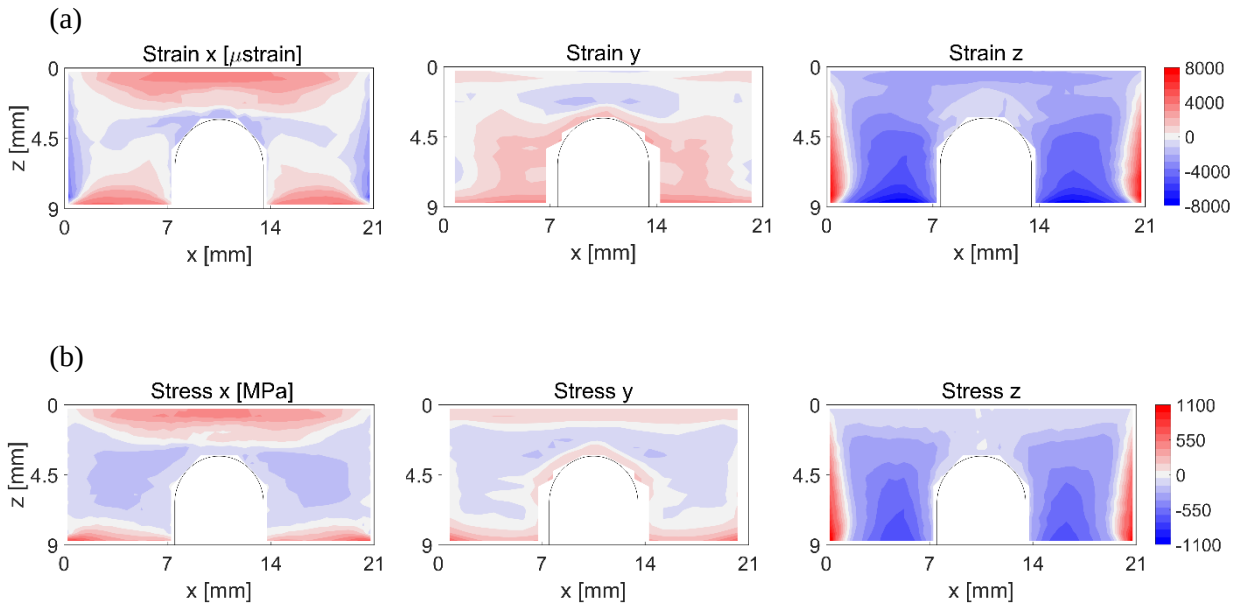

Figure 3: Simulation predictions of the (a) residual strain maps over the investigated middle cross-section (y = 2.5 mm) of the sample. Strains are shown in μstrain for the x, y and z strain components. (b) Residual stress maps over the investigated middle cross-section of the sample. Stresses are shown in MPa.

In an effort to quantitatively compare the experimental measurements with the simulation predictions, line-outs of the measured and simulated contour plots were produced, as shown in Figure 4. The measured strains are shown in black and the simulated strains in red. Line-outs were extracted along the height at x = 3.75 mm and along two different lengths at z = 6.25 mm and z = 1.25 mm.

The comparison between the measured data and the predictions is done by using explicitly the strain results (Fig. 2(a) and Fig. 3(a)). During the measurements of the x and z components, the integration volume is 0.2 mm × 1.5 mm × 0.2 mm in x, y and z respectively. The extended diffraction volume could degrade the resolution of the measurement. However, we do not expect large through-thickness variations in the y

direction of the sample. On the other hand, for the measurement of the y strain component, the integration volume is 1.5 mm × 0.2 mm × 0.2 mm in x, y and z, respectively. In the case of the y strain component, the long dimension of the diffraction volume is located along the x dimension of the sample where we expect stronger gradients. As one can see from Hooke's law (Eq. 2), any stress component is coupled to all the three orthogonal strain components. Consequently, in order to calculate the stresses, we essentially degrade the resolution from 0.2 mm to 1.5 mm on all three stress components (x, y and z). This is why we use strain instead of stress for these comparisons.

Figure 4(a) shows line-out plots of the x, y, and z components of the residual strains at x = 3.75 mm. The predicted strains (in red) show very good agreement with the measured strains (in black). The x component of the strains (see Figure 4(a) a.x) is roughly zero in the interior of the sample while strains tensile at the top and bottom of the sample. The y strains (see a.y) are mainly tensile and exhibit a small change along the height of the sample. On the other hand, the z strain component (a.z) indicates a steeper gradient in the strain. High compressive strain is present close to the substrate while close to the top of the sample the strain approaches zero. Figure 4(b), shows the line-out profiles of the three strain components as extracted along the length of the bridge at z = 6.25 mm. It is apparent that the x strain (see b.x) exhibits a reversed flattened parabolic distribution within the legs of the bridges –larger compressive values at the free edge balanced by small compressive and close to zero strains within the sample. The y strain component (b.y) indicates a similar trend with a more modest change in strains along the 21 mm length of the sample. However, the z strain component (b.z) indicates an opposing trend, high tensile strain (8,000 με) at the free edges and high compressive strains (~ 4,000 με) in the interior. Similar strain distributions are observed for the case of z = 1.25 mm with the difference that the strain magnitude is increased drastically (maximum strain ≈ 3,000 με).

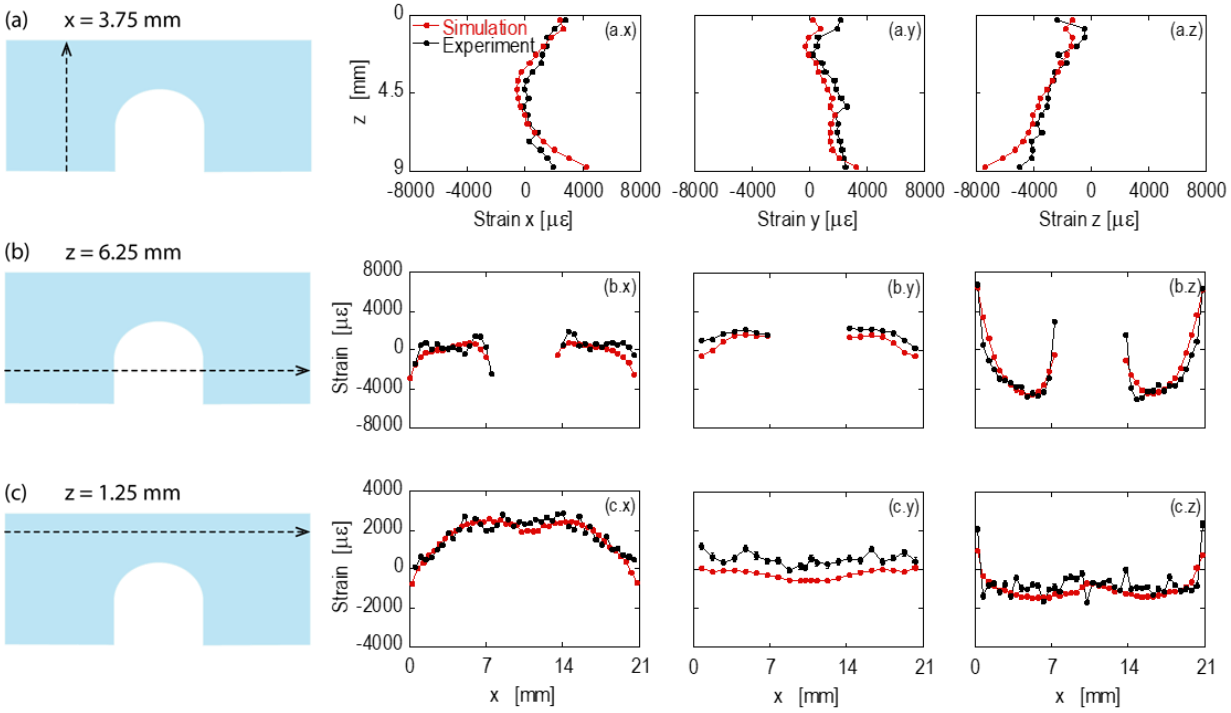

Figure 4: Comparison between measured and simulated strains. (a) Line-out profile of the residual strains at x = 3.75 mm; (b) residual strain line-out profile at z = 6.25 mm and (c) residual strain line-out profile at z = 1.25 mm. Simulation predictions are shown in red and experimental measurements are shown in black. The uncertainty of the experimental measurements is covered by the symbols.

It is obvious that the model well predicts the large gradient in the z-component of the strain observed at z = 6.25mm and z = 1.25 mm. Note that the simulations tend to over-predict the strains near the substrate,

especially in the x and z directions (see Figure 4(a)). The over-prediction of strains near the bottom portion of the bridges may be explained by the constant temperature, Dirichlet boundary condition applied to the bottom of the computational base plate. In reality, the base plate would heat up as the part is built. Accurate temperature measurements of the base plates were not available and the researchers wanted to avoid a "fitting" approach where parameters are purposely tuned to match the experimental measurements. Other sources of error can be attributed to uncertainty in the exact material properties and not capturing the exact thermal history of all points in the part due to the agglomeration methodology used. For the current specimen, there is good overall agreement exhibited between the residual strains measured via X-ray diffraction and the Diablo simulations. The predicted strains show the same trends as the experimental measurements and are quantitatively comparable. Future extended investigations will present the residual stress distribution of different scan patterns where the simulation predictions do not exhibit an overall good agreement.

In summary, this work shows that it is possible to successfully determine the three-dimensional residual strain and stress distribution in Ti-6Al-4V L-PBF samples by means of high-energy X-ray diffraction. High-energy X-ray diffraction is a useful tool that can provide rigorous measurements and provide valuable information for predictive computational codes, such as Diablo. The presented experimental measurements offered a strong validation of the simulation code, allowing for increased confidence in the ability of this code to predict the residual stress state within a Ti-6Al-4V L-PBF part. This work is important not only in regard to understanding the residual stress distribution within AM samples, but also by providing for engineering relevance with respect to the certification of L-PBF components in safety critical applications.

Acknowledgement

This work was performed under the auspices of the U.S. Department of Energy by Los Alamos National Laboratory under the contract DE-AC52-06NA25396 and by Lawrence Livermore National Laboratory under Contract DE-AC52-07NA27344. The experimental results of the current work are based upon research conducted at the Cornell High Energy Synchrotron Source (CHESS), which is supported by the National Science Foundation under award DMR-1332208.

References

[1] A. Prijan, D.-M. Petrosanu, J. Inf. Syst. Oper. Manag. (2013) 1–11.
[2] T. Wohlers, T. Gornet, Wohlers Rep. 2014 (2014) 1–23.
[3] K. V. Wong, A. Hernandez, ISRN Mech. Eng. 2012 (2012) 1–10.
[4] E. Atzeni, A. Salmi, Int. J. Adv. Manuf. Technol. 62 (2012) 1147–1155.
[5] L. Wang, S.D. Felicelli, P. Pratt, Mater. Sci. Eng. A 496 (2008) 234–241.
[6] B. Vrancken, V. Cain, R. Knutsen, J. Van Humbeeck, Scr. Mater. 87 (2014) 29–32.
[7] I.D. Parsons, J.M. Solberg, R.M. Ferencz, M.A. Havstad, N.E. Hodge, A.P. Wemhoff, Diablo User Manual. UCRL-SM-234927, 2007.
[8] Y.M. Wang, Mechanical Properties of Ti-6Al-4V Samples Produced by Laser Poweder Bed Fusion, Livermore, 2016.
[9] J.C. Mach, C.J. Budrow, D.C. Pagan, J.P.C. Ruff, J.S. Park, J. Okasinski, A.J. Beaudoin, M.P. Miller, Jom 69 (2017) 893–899.
[10] B. Clausen, SMARTSware Manual, Los Alamos National Lab, Los Alamos, NM, 2004.
[11] A.C. Larson, R.B. Von Dreele, GSAS Manual, Los Alamos National Lab, Los Alamos, NM, 1986.
[12] M.R. Daymond, M.A.M. Bourke, R.B. Von Dreele, B. Clausen, T. Lorentzen, J. Appl. Phys. 82 (1997) 1554–1562.
[13] M.R. Daymond, M.A.M. Bourke, R.B. Von Dreele, J. Appl. Phys. 85 (1999) 739–747.
[14] N.E. Hodge, R.M. Ferencz, J.M. Solberg, Comput. Mech. 54 (2014) 33–51.

[15] N.E. Hodge, R.M. Ferencz, R.M. Vignes, Addit. Manuf. 12 (2016) 159–168.
[16] C.C. Murgau, Microstructure Model for Ti-6Al-4V Used in Simulation of Additive Manufacturing. Ph.d. Dissertation, Lulea Unversity of Technology, 2016.
[17] J. Goldak, J. Zhou, V. Breiguine, MontoyaF., Trans. JWRI 2 (1996) 185–189.
[18] P. Rangaswamy, M.L. Griffith, M.B. Prime, T.M. Holden, R.B. Rogge, J.M. Edwards, R.J. Sebring, Mater. Sci. Eng. A 399 (2005) 72–83.
[19] P. Mercelis, J.-P. Kruth, Rapid Prototyp. J. 12 (2006) 254–265.